Exploiting Correlation With Wideband CQI and Making Differential Feedback Overhead Flexible in 4G/5G OFDM Systems

Vineeth Kumar⬛ and Neelesh B. Mehta⬛, *Fellow, IEEE*

Abstract—**Differential channel quality indicator (CQI) and wideband CQI are key components of the reduced feedback schemes employed in the 5G New Radio (NR) and 4G Long Term Evolution (LTE) standards. They enable a base station (BS) to acquire channel state information that is essential for rate adaptation and frequency-domain scheduling without overwhelming the uplink. We present a novel throughput-optimal rate adaptation rule that exploits the correlation between the differential and wideband CQIs to improve throughput without any additional feedback. It also shows that the prevalent conventional method that adds the two CQIs is sub-optimal. We then propose a novel flexible-overhead differential CQI feedback scheme, in which the number of bits for differential CQI can be different across the subbands. This provides a new flexibility to the BS to control the feedback overhead. It differs from the current rigid parameterization, in which a user always feeds back a 2-bit differential CQI for each subband. In various single-user and multi-user deployment scenarios involving small-scale fading, large-scale shadowing, and co-channel interference, the proposed approach achieves nearly the same throughput as the feedback scheme employed in 5G and LTE, but with much less overhead.**

Index Terms—**5G new radio, long term evolution, discrete rate adaptation, channel quality indicator, exponential effective SNR mapping, OFDM, scheduling.**

I. INTRODUCTION

THE 4G Long Term Evolution (LTE) and the 5G new radio (NR) standards use orthogonal frequency division multiplexing (OFDM) as the physical layer access technology on the downlink [2], [3]. In order to achieve high spectral efficiencies, these standards divide the system bandwidth into orthogonal subcarriers and employ techniques such as rate adaptation, frequency-domain scheduling, and multiple-input-multiple-output (MIMO) [2].

Differential channel quality indicator (CQI) feedback, which is also referred to as *higher layer-configured subband* (HLCS)

feedback, is a critical component of both 4G LTE and 5G NR. It provides the channel state information that is essential for frequency-domain scheduling and rate adaptation by the base station (BS), while controlling the feedback overhead on the resource-limited uplink feedback channel. In HLCS feedback, CQI is fed back at the frequency resolution of a subband. A subband comprises 24-96 adjacent subcarriers in 4G and 48-384 adjacent subcarriers in 5G. The CQI is fed back as wideband CQI and differential CQI. The wideband CQI, which consists of only 4 bits, is the index of the modulation and coding scheme (MCS) that can be reliably decoded if the entire system bandwidth is allocated to that user. For each subband, the differential CQI encodes using 2 bits the difference between the index of the MCS that the user can reliably decode on that subband and the wideband CQI.

The larger bandwidths and the larger number of users that need to be serviced have led to feedback overhead becoming a significant bottleneck in the uplink. This is despite the above steps taken to control it [4], [5]. Given its practical importance, this issue has attracted considerable attention in the literature, which we summarize below. We do not delve into the feedback schemes for MIMO or millimeter-wave communications since they are based on a different set of principles.

A. Prior Works on Subband-Level CQI Feedback

Subband-level CQI feedback schemes, which are closely related to the HLCS feedback scheme, have been studied in [4]–[11]. In these schemes, CQI is fed back at the frequency-domain resolution of a subband. In [6], the throughput of subband-level CQI feedback when used in conjunction with multi-user (MU)-MIMO is studied, but only via simulations. In [8], subband-level CQI is used for allocating user pairs to subbands in a non-orthogonal multiple access system. In [7], its throughput with carrier aggregation is studied via simulations. In [9], subband-level CQI is used to design a scheduling algorithm that enhances the throughput while still adhering to quality-of-service constraints in a multicast network. In [10], the throughput of subband-level CQI feedback is analyzed for a single-cell, multi-user scenario. In [12], the spatial correlation of large-scale shadowing is utilized to restrict the number of users that feed back CQI. However, the above works do not model differential encoding, which is a key element of HLCS feedback.

In [4], Gaussian process regression is used to predict future CQI values and send the HLCS feedback less often. This is improved upon using predictive filters in [5]. In [11], expressions for the throughput of the HLCS feedback scheme are derived for a multi-cell, multi-user scenario. However, these works assume full channel state information [6]–[10] or employ the conventional MCS selection rule (C-MSR) in which the BS adds the wideband and differential CQIs to determine the index of the transmit MCS of each subband [4], [5], [11].

B. Focus and Contributions

In this paper, we present two innovations. We first propose a *throughput-optimal MCS selection* (TOMS) rule that exploits the correlation between the wideband and differential CQIs to improve rate adaptation. We then propose a novel differential CQI feedback scheme for the sub-6 GHz bands of operation. It employs a novel combination of the wideband and differential CQIs and applies the TOMS rule. In it, the number of bits used for differentially encoding the CQI can be different for different subbands. This gives the BS a new flexibility to control the total feedback overhead, for example, as a function of the loading in the cell. We make the following contributions:

- We propose a novel TOMS rule for the BS that specifies the throughput-optimal MCS to use in each subband given the wideband and differential CQIs. It exploits the correlation that is inherent between these two CQIs. The correlation occurs because the wideband CQI depends on each subband's signal-to-interference-plus-noise ratio (SINR). Furthermore, the large-scale shadowing and path-loss are the same for all subbands, even though the small-scale fading is not. To the best of our knowledge, this correlation has not been exploited in the literature. We also highlight the sub-optimality of C-MSR [4], [5], [11].

- We derive novel closed-form expressions for the *feedback-conditioned goodput* of an MCS, which the TOMS rule maximizes, as a function of the wideband and differential CQIs. The expressions reduce the complexity of implementing the TOMS rule. We derive them for the following three widely studied deployment scenarios: (i) Scenario with path-loss, small-scale fading, and noise [10], [13], [14], (ii) Scenario with path-loss, small-scale fading, large-scale shadowing, and noise [11], [15], [16], and (iii) Scenario with path-loss, small-scale fading, large-scale shadowing, co-channel interference, and noise [9], [15], [17]. The first scenario is also relevant when the standard deviation of lognormal shadowing is small [18]. The second and third scenarios capture the randomness due to shadowing, which is different for different links and users. Our expressions apply to many single-stream MIMO, single-user multi-stream MIMO, and MU-MIMO modes.

- We propose a subband-level, flexible-overhead differential CQI feedback scheme. It feeds back the wideband CQI using 4 bits, but the number of bits for differential CQI can be different for different subbands. It differs from HLCS feedback, in which a user always feeds back 2 bits per subband for differential CQI. Intuitively, the wideband CQI tracks path-loss and large-scale shadowing, which are the same for all subbands in the bandwidths typical in sub-6 GHz deployments. The differential CQI tracks the small-scale fading at a finer subband level. This judicious combination of wideband and differential CQIs, which are already adopted in the standards, and the TOMS rule ensures that minimal modifications are needed for the proposed feedback scheme to be implemented.

- Our comprehensive benchmarking shows that our approach achieves the same or higher throughput than HLCS feedback with significantly less feedback overhead in all the above scenarios.

Comments: Our approach differs from differential feedback for MIMO-OFDM systems in [13] and the references therein because these works do not model salient aspects of the 4G and 5G standards such as differential and wideband CQIs, and rate adaptation. Differential techniques have been extensively investigated in classical areas such as quantization [19, Ch. 3] and modulation [19, Ch. 5]. However, our cellular system model and problem formulation are different, require novel analytical tools, and lead to a different solution. Our approach also differs from the BS-side estimation technique in [20], which did not consider differential feedback. Only a throughput analysis of the conventional HLCS feedback scheme with C-MSR is developed in [11]. Our approach, which focuses on reducing the frequency-domain feedback overhead, is complementary to the approaches in [4] and [12], which exploit correlations in time and spatial domains.

C. Organization and Notation

This paper is organized as follows. Section II presents the system model. Section III develops the TOMS rule for different scenarios. Numerical results are presented in Section IV. Our conclusions follow in Section V.

Notation: We denote the probability of an event A by $\Pr(A)$ and the joint probability of events A and B by $\Pr(A, B)$. The conditional probability of A given B is denoted by $\Pr(A \mid B)$. We denote the probability density function (PDF) of a random variable (RV) X by $f_X(\cdot)$, its cumulative distribution function (CDF) by $F_X(\cdot)$, and the expectation with respect to X by $\mathbb{E}_X[\cdot]$. We denote the complex conjugate of a by a^* and its absolute value by $|a|$. Vectors and matrices are denoted using bold-face characters. For a matrix $\mathbf{H}$, we denote its Hermitian transpose by $\mathbf{H}^\dagger$. The indicator function $1_{\{a\}}$ equals 1 if a is true, else it is 0.

II. 4G/5G DOWNLINK BASICS AND SYSTEM MODEL

We consider the following system model that captures several key aspects of the OFDM-based cellular downlink in 4G LTE and 5G NR systems. We treat the two systems together given the commonalities in their design in the sub-6 GHz bands. We also highlight the differences between them in the discussion below. A group of adjacent subcarriers constitutes a physical resource block (PRB). q adjacent PRBs constitute a subband. Let the number of subbands be B. Then, the number

of PRBs is qB. For example, in LTE, a subcarrier has a bandwidth of 15 kHz. In 5G NR, the subcarrier bandwidth instead varies from 15 kHz to 240 kHz [21]. In both standards, a PRB comprises 12 subcarriers and a subband comprises 2 to 8 PRBs.

A BS serves K users in the reference cell 0, which receives co-channel interference from C neighboring cells. The BS has N_t transmit antennas and each user has N_r receive antennas.

A. Channel Model

1) Small-Scale Fading: $\mathbf{H}_{kn}^{(c)}$ is an $N_r \times N_t$ matrix, whose $(i,j)^{\text{th}}$ element $H_{kn}^{(c)}(i,j)$ denotes the complex downlink baseband fading gain on subband n of user k between transmit antenna j of BS c and receive antenna i of the user, where $1 \leq i \leq N_r$, $1 \leq j \leq N_t$, $1 \leq n \leq B$, $1 \leq k \leq K$, and $0 \leq c \leq C$. With Rayleigh fading, $H_{kn}^{(c)}(i,j)$ is a circularly-symmetric complex Gaussian RV with unit variance. For subband n, $H_{kn}^{(c)}(i,j)$ are independent and identically distributed (i.i.d.) for different i and j [22, Ch. 2]. $H_{k1}^{(c)}(i,j), \ldots, H_{kB}^{(c)}(i,j)$ are statistically identical but correlated [23, Ch. 3]. To model this correlation, we employ the widely used exponential correlation model, in which the covariance of $H_{kn}^{(c)}(i,j)$ and $H_{kn'}^{(c)}(i,j)$ is $\rho^{2|n-n'|}$, where $0 \leq \rho \leq 1$ [24], [25]. Later, we show how our approach can also be applied to an arbitrary correlation model.

2) Large-Scale Shadowing and Path-Loss: The large-scale shadowing of the channel between user k and BS c is denoted by ω_{ck}. It is the same for all subbands [22, Ch. 1]. In dB scale, ω_{ck} is a Gaussian RV with mean $\mu_{\omega_{ck}}(x_{ck}) = -\delta_{\text{dB}}(x_0) - 10\eta \log_{10}(x_{ck}/x_0)$, which models path-loss, and standard deviation σ_{shad}. Here, x_{ck} is the distance between BS c and user k, $\delta_{\text{dB}}(x_0)$ is the path-loss in dB at a reference distance x_0 from the BS, and η is the path-loss exponent. This model captures the heterogeneity in shadowing and path-loss across users in both signal and interference terms.

3) SINR for Different Multi-Antenna Modes: To simplify notation, we henceforth drop the cell-index for all variables associated with the users in the reference cell 0. Therefore, we use ω_k instead of ω_{0k}, Ω_k instead of Ω_{0k}, and so on. The following expression for the SINR γ_{kn} on subband n of user k in the reference cell applies to several multi-antenna modes [11], [26]:

$$\gamma_{kn} = \frac{P_T \omega_k}{P_N \varepsilon_{kn}} \phi_{kn} = \Omega_k \phi_{kn}, \qquad (1)$$

where

$$\Omega_k = \frac{P_T \omega_k}{P_N \varepsilon_{kn}}, \qquad (2)$$

$$\varepsilon_{kn} = \frac{P_T}{P_N} \sum_{c=1}^{C} \omega_{ck} |I_{kn}(c)|^2 + 1. \qquad (3)$$

Here, P_T is the BS transmit power per subband, P_N is additive white Gaussian noise (AWGN) power per subband, ω_{ck} is the path-loss and large-scale shadowing from BS c to user k, ϕ_{kn} is the small-scale fading on subband n between BS 0 and user k, and $I_{kn}(c)$ is the small-scale fading of the interfering signal from BS c to user k on subband n.
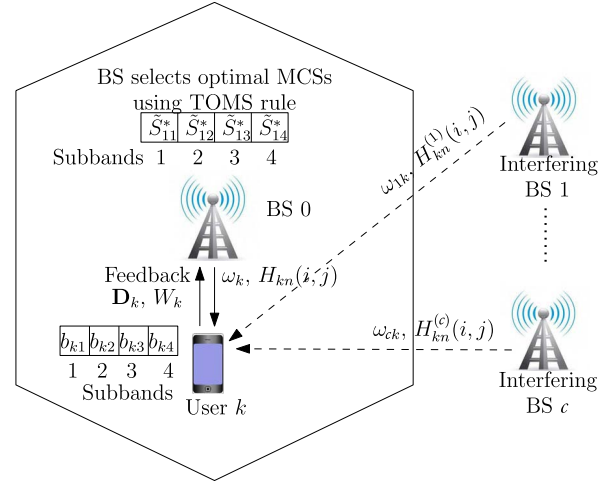

Fig. 1. Illustration of channel model, subbands, flexible-overhead differential CQI feedback, and the TOMS rule ($B = 4$).

B. Discrete Rate Adaptation and CQI Feedback

The BS has an *MCS set* $\mathcal{M} = \{1, 2, \ldots, M\}$ of M MCSs. In it, MCS m has a rate r_m and a decoding threshold T_m. User k can decode it on subband n if $\gamma_{kn} \geq T_m$. Else, an outage occurs [10], [27]. Without loss of generality, let $0 = r_1 < r_2 < \cdots < r_M$ and $0 = T_1 < T_2 < \cdots < T_M < T_{M+1} = \infty$. User k determines from γ_{kn} the subband CQI Q_{kn} as follows. It is the index of the highest-rate MCS that it can reliably decode on subband n, i.e.,

$$Q_{kn} = m, \quad \text{if } T_m \leq \gamma_{kn} < T_{m+1}. \qquad (4)$$

For example, in LTE, there are $M = 2^4 = 16$ CQIs, whose MCSs and rates are tabulated in [2, Table 10.1]. LTE supports QPSK, 16QAM, and 64QAM modulation schemes and the rates after channel coding range from 0.15 to 5.55 bits/symbol. In 5G, there are three such MCS tables [3]. 5G also supports 256QAM. The SINR γ_{kn} can be estimated by the user using the reference signals it receives from the BSs. In our analysis, we assume that the estimation error at the receiver is negligible [26], [28].

The wideband CQI W_k is the index of the highest-rate MCS such that a codeword transmitted using it over the entire system bandwidth can be reliably decoded by user k [2, Ch. 10]. Unlike the subband CQI, W_k is a single number that is reported for the entire bandwidth even though different subbands experience different, albeit correlated, fades in a frequency-selective channel. To systematically determine W_k, we use the exponential effective signal-to-noise-ratio (SNR) mapping (EESM). It has been used in analyses and system-level simulations of cellular standards [4], [28], [29]. It maps the vector of subband SNRs $\boldsymbol{\gamma}_k = (\gamma_{k1}, \ldots, \gamma_{kB})$ seen by a codeword transmitted over B subbands into a single effective SNR $\zeta_k^{(m)}$ for MCS m as follows:

$$\zeta_k^{(m)} = -\beta_m \log\left(\frac{1}{B} \sum_{n=1}^{B} \exp\left(-\frac{\gamma_{kn}}{\beta_m}\right)\right), \quad \text{for } m \geq 2, \quad (5)$$

where β_m is an MCS-dependent scaling constant [4], [29]. $\zeta_k^{(m)}$ is interpreted as the equivalent SNR for MCS m that results in the same probability of error in an AWGN channel.

TABLE I
DETERMINATION OF DIFFERENTIAL CQI
GIVEN THE NUMBER OF FEEDBACK
OVERHEAD BITS

b_{kn} (bits)	D_{kn}	Condition	b_{kn} (bits)	D_{kn}	Condition
1	0	$\Delta_{kn} \leq 0$		-3	$\Delta_{kn} \leq -3$
	1	$\Delta_{kn} > 0$		-2	$\Delta_{kn} = -2$
2	-1	$\Delta_{kn} \leq -1$		-1	$\Delta_{kn} = -1$
	0	$\Delta_{kn} = 0$	3	0	$\Delta_{kn} = 0$
	1	$\Delta_{kn} = 1$		1	$\Delta_{kn} = 1$
	2	$\Delta_{kn} \geq 2$		2	$\Delta_{kn} \geq 2$
-	-	-		3	$\Delta_{kn} = 3$
				4	$\Delta_{kn} \geq 4$

W_k is then the highest-rate MCS for which $\zeta_k^{(m)} \geq T_m$. Thus, for $2 \leq m \leq M$,

$$W_k = m \text{ if and only if}$$
$$\zeta_k^{(m)} \geq T_m, \zeta_k^{(m+1)} < T_{m+1}, \ldots, \zeta_k^{(M)} < T_M. \quad (6)$$

Else, $W_k = 1$, which corresponds to the zero rate (r_1).

1) Flexible-Overhead Differential CQI Feedback: We propose that user k encodes the difference $\Delta_{kn} = Q_{kn} - W_k$ for subband n using $b_{kn} \in \{0, 1, 2, 3, 4\}$ bits. The maximum of 4 bits arises because only 16 MCSs are defined for feedback in LTE and 5G [2, Ch. 10], [3]. Let the encoded value be D_{kn}, which we shall refer to as the differential CQI for subband n of user k. The values it can take depend on b_{kn}.

The proposed encoding scheme for $b_{kn} \in \{1, 2, 3\}$ is specified in Table I.[1] (i) For $b_{kn} = 1$ bit, if $\Delta_{kn} \leq 0$, then $D_{kn} = 0$. Else, $D_{kn} = 1$. (ii) For $b_{kn} = 2$ bits, if $\Delta_{kn} \leq -1$, then $D_{kn} = -1$. If $\Delta_{kn} = 0$, then $D_{kn} = 0$. If $\Delta_{kn} = 1$, then $D_{kn} = 1$. Else, if $\Delta_{kn} \geq 2$, then $D_{kn} = 2$. This encoding is kept the same as that in HLCS feedback [2, Ch. 10]. The encoding for $b_{kn} = 3$ bits is specified in a similar manner. We refer to $\mathbf{D}_k = (D_{k1}, \ldots, D_{kB})$ as the vector of differential CQIs and $\mathbf{b}_k = (b_{k1}, b_{k2}, \ldots, b_{kB})$ as the *overhead bit pattern (OBP)*.

The user feeds back $\mathbf{D}_k$ and W_k to the BS. Hence, the total differential feedback overhead for user k is $O_k = \sum_{n=1}^{B} b_{kn}$ bits and the total feedback overhead including the 4-bit wideband CQI is $(O_k + 4)$ bits. This system model illustrated in Fig. 1.

2) Implementation Aspects: The BS chooses the OBP $\mathbf{b}_k$ and communicates it to the user. It is important to note that this needs to be done only occasionally, i.e., every few tens of seconds. For example, the BS can do this when the loading in the cell changes. Thus, higher-layer radio resource control signaling suffices for implementing it. We note that in LTE and 5G, HLCS feedback is only permitted for aperiodic feedback due to its higher overhead [2, Ch. 10]. Our scheme can enable differential CQI feedback to be used even for periodic feedback since its overhead can be controlled by the BS.

---

[1]Two extreme cases need a special mention. First, for $b_{kn} = 4$ bits, Q_{kn} is reported as is without differential encoding since 4 bits are sufficient to indicate one among the 16 MCSs in the MCS table. Second, for $b_{kn} = 0$ bits, no feedback is sent for subband n.

III. OPTIMAL MCS SELECTION RULE & FEEDBACK-CONDITIONED GOODPUT

We now determine the throughput-optimal downlink MCS $\tilde{S}_{kn}^*$ for subband n of user k given the wideband CQI W_k and the vector of differential CQIs $\mathbf{D}_k$.

The rate achieved when MCS m is chosen is equal to $r_m 1_{\{\gamma_{kn} \geq T_m\}}$ because the user can decode it only if $\gamma_{kn} \geq T_m$. Therefore, the throughput conditioned on $\mathbf{D}_k$ and $W_k = w$ is

$$\mathbb{E}\left\{r_m 1_{\{\gamma_{kn} \geq T_m\}} \mid \mathbf{D}_k, W_k = w\right\}$$
$$= r_m \Pr(\gamma_{kn} \geq T_m \mid \mathbf{D}_k, W_k = w). \quad (7)$$

Let $\Psi_{kn}^{(m)}(\mathbf{D}_k, w) = r_m \Pr(\gamma_{kn} \geq T_m \mid \mathbf{D}_k, W_k = w)$. We shall refer to it as the *feedback-conditioned goodput* of MCS m on subband n. Hence, the throughput-optimal MCS $\tilde{S}_{kn}^*$ for subband n is

$$\tilde{S}_{kn}^* = \arg\max_{m \in \mathcal{M}} \left\{\Psi_{kn}^{(m)}(\mathbf{D}_k, w)\right\}. \quad (8)$$

Thus, $\tilde{S}_{kn}^*$ is the index of the MCS that maximizes the feedback-conditioned goodput. We refer to this as the TOMS rule. C-MSR is sub-optimal since it determines the MCS $\tilde{S}_{kn}$ for subband n differently as

$$\tilde{S}_{kn} = W_k + D_{kn}. \quad (9)$$

The main challenge lies in deriving an expression for $\Psi_{kn}^{(m)}(\mathbf{D}_k, w)$ that is tractable and has a low computational complexity. We set up the problem below. Given D_{kn} and $W_k = w$, it follows that $\gamma_{kn} \in [L_k(n), U_k(n))$, where $L_k(n)$ and $U_k(n)$ are the lower and upper thresholds of the SINR region in which γ_{kn} lies.[2] This region can be easily inferred as follows: (i) From Table I, the BS identifies the condition for Δ_{kn} that corresponds to the given value of b_{kn} and the fed back D_{kn}. (ii) The condition in Δ_{kn} translates into a corresponding condition for Q_{kn} since $Q_{kn} = w + \Delta_{kn}$ (cf. Section II-B.1). (iii) From the condition for Q_{kn}, the BS then determines the range in which γ_{kn} lies using (4). For example, $b_{kn} = 2$ bits and $D_{kn} = -1$ imply that $\Delta_{kn} \leq -1$. This, in turn, implies that $Q_{kn} \leq w - 1$. From (4), we then get $0 \leq \gamma_{kn} < T_w$. Similarly, for $b_{kn} = 2$ bits and $D_{kn} = 0$, we get $Q_{kn} = w$ and $T_w \leq \gamma_{kn} < T_{w+1}$.

Substituting the SINR regions for $\gamma_{k1}, \ldots, \gamma_{kB}$ in (7) yields

$$\Psi_{kn}^{(m)}(\mathbf{D}_k, w) = r_m \Pr(\gamma_{kn} \geq T_m \mid L_k(1) \leq \gamma_{k1} < U_k(1),$$
$$\ldots, L_k(B) \leq \gamma_{kB} < U_k(B), W_k = w). \quad (10)$$

Applying Bayes' rule, we get

$$\Psi_{kn}^{(m)}(\mathbf{D}_k, w) = r_m \frac{\Pr(\gamma_{kn} \geq T_m, L_k(1) \leq \gamma_{k1} < U_k(1), \\ \ldots, L_k(B) \leq \gamma_{kB} < U_k(B), W_k = w)}{\Pr(L_k(1) \leq \gamma_{k1} < U_k(1), \\ \ldots, L_k(B) \leq \gamma_{kB} < U_k(B), W_k = w)}. \quad (11)$$

Note that the expression for $\Psi_{kn}^{(m)}(\mathbf{D}_k, w)$ in (11) depends on the statistics of the signal and interference-plus-noise terms, which, in turn, depend on the deployment scenario under consideration.

---

[2]For the special case of $b_{kn} = 0$ bits, $\gamma_n \in [0, \infty)$.

We now compute $\Psi_{kn}^{(m)}(\mathbf{D}_k, w)$ separately for the aforementioned three scenarios. We employ novel scenario-specific approximations that simplify the expression for $\Psi_{kn}^{(m)}(\mathbf{D}_k, w)$. In the scenarios with shadowing, we reduce it to a ratio consisting of a sum or difference of probability terms involving an effective SNR (or SINR) and a subband SNR (or SINR). We then employ several techniques from the literature to compute these terms.

A. Scenario With Path-Loss, Small-Scale Fading, and Noise

In this scenario, the post-processing SNR on subband n of user k in cell 0 takes the following unified form:

$$\gamma_{kn} = \bar{\gamma}_k \phi_{kn}, \tag{12}$$

where $\bar{\gamma}_k = (P_T \delta(x_0)/P_N)(x_k/x_0)^{-\eta}$ is the mean SNR of user k and ϕ_{kn} tracks the small-scale fading. ϕ_{kn} is a gamma RV with PDF $f_{\phi_{kn}}(v) = v^{d_k-1} \exp(-v/\varphi_k)/(\Gamma(d_k)\varphi_k^{d_k})$, for $v \geq 0$, where $\Gamma(\cdot)$ is the gamma function [30, (8.310)], d_k is its shape parameter, and φ_k is its scale parameter. It applies to single-input-multiple-output (SIMO) with maximal ratio combining (MRC), multiple-input-single-output (MISO) with maximal ratio transmission (MRT), and single-stream MIMO with singular value decomposition (SVD)-based beamforming as follows [31]:

- *SIMO with MRC:*[3] $d_k = N_r$ and $\varphi_k = 1$ because $\phi_{kn} = \sum_{i=1}^{N_r} |H_{kn}(i,1)|^2$.
- *MISO with MRT:* $d_k = N_t$ and $\varphi_k = 1$ because $\phi_{kn} = \sum_{j=1}^{N_t} |H_{kn}(1,j)|^2$.
- *Single-stream MIMO with Beamforming:* $d_k = N_r N_t$ and $\varphi_k = ((N_t + N_r)/(N_t N_r + 1))^{\frac{2}{3}}$ [31].

To compute the probabilities in the numerator and denominator of (11), we need the joint PDF of the B subband SNRs $\gamma_{k1}, \ldots, \gamma_{kB}$ and the M effective SNRs $\zeta_k^{(1)}, \ldots, \zeta_k^{(M)}$, which together determine w. However, such a PDF is intractable. In fact, even the marginal distribution of $\zeta_k^{(m)}$ is not known in closed-form. This problem can be addressed by noticing that the information conveyed by W_k is also captured in the SNR regions for $\gamma_{k1}, \ldots, \gamma_{kB}$. This is because the large-scale fading, on which W_k depends, is also captured by the SNR regions since the differential CQI for each subband is generated by subtracting W_k from the subband's MCS index. This motivates the following approximation, in which the conditioning on $W_k = w$ in (10) is dropped and then the Bayes' rule is applied:

$$\Psi_{kn}^{(m)}(\mathbf{D}_k, w) \approx r_m \frac{\begin{array}{c}\Pr(\gamma_{kn} \geq T_m, L_k(1) \leq \gamma_{k1} < U_k(1),\\ \ldots, L_k(B) \leq \gamma_{kB} < U_k(B))\end{array}}{\begin{array}{c}\Pr(L_k(1) \leq \gamma_{k1} < U_k(1),\\ \ldots, L_k(B) \leq \gamma_{kB} < U_k(B))\end{array}}. \tag{13}$$

We shall see in Section IV-C that this is accurate for a wide range of values of ρ from 0 to 0.9.

1) Computational Complexity and Its Reduction: The joint PDF $f_{\boldsymbol{\gamma}_k}(\cdot)$ of $\boldsymbol{\gamma}_k = (\gamma_{k1}, \ldots, \gamma_{kB})$, which is needed to compute the numerator and denominator in (13), is given

[3] The expression for SINR for single-input-single-output (SISO) is a special case of SIMO. We do not show it separately.

by [24]

$$f_{\boldsymbol{\gamma}_k}(u_1, \ldots, u_B) = \frac{e^{\frac{-d_k}{\bar{\gamma}_k(1-\rho^2)}\left(u_1 + u_B + (1+\rho^2)\sum_{i=2}^B u_i\right)}}{(\frac{\bar{\gamma}_k}{d_k})^{d_k B} \Gamma(d_k)(1-\rho^2)^{d_k(B-1)}}$$
$$\times \sum_{t=0}^{\infty} \left(\frac{d_k \rho}{\bar{\gamma}_k(1-\rho^2)}\right)^{2t}$$
$$\times \sum_{\substack{\nu_1 \geq 0, \ldots, \nu_{B-1} \geq 0 \\ \nu_1 + \cdots + \nu_{B-1} = t}} \left[\prod_{j=2}^{B-1} \frac{(u_j)^{\nu_i + \nu_{i-1} + d_k - 1}}{\nu_j \Gamma(\nu_j + d_k)}\right]$$
$$\times \frac{(u_B)^{\nu_{B-1} + d_k - 1}}{\Gamma(\nu_1 + d_k) \nu_1(u_1)^{1-\nu_1-d_k}},$$
$$\text{for } u_1 \geq 0, \ldots, u_B \geq 0. \tag{14}$$

The complexity in computing the tth term in the above series is $\mathcal{O}\left(\binom{B+t-2}{t}\right)$ because of the summation $\sum_{\substack{\nu_1 \geq 0, \ldots, \nu_{B-1} \geq 0 \\ \nu_1 + \cdots + \nu_{B-1} = t}}$. It rapidly increases as t or B increases.

The complexity can be significantly reduced by computing $\Psi_{kn}^{(m)}(\mathbf{D}_k, w)$ using only the CQI of the $2N_w$ adjacent subbands whose indices lie between $n - N_w$ and $n + N_w$. Let n^- and n^+ denote the smallest and the largest indices, respectively, of the subbands that are used to compute $\Psi_{kn}^{(m)}(\mathbf{D}_k, w)$. Since n varies from 1 to B, the following three conditions can occur:
1) $n - N_w \leq 0$ *and* $n + N_w \leq B$: In this case, $n^- \triangleq 1$ and $n^+ \triangleq n + N_w$.
2) $n - N_w > 0$ *and* $n + N_w \leq B$: In this case, $n^- \triangleq n - N_w$ and $n^+ \triangleq n + N_w$.
3) $n - N_w > 0$ *and* $n + N_w > B$: In this case, $n^- \triangleq n - N_w$ and $n^+ \triangleq B$.

Therefore, (13) can be compactly written as follows for all the three conditions:

$$\Psi_{kn}^{(m)}(\mathbf{D}_k, w) \approx r_m \frac{\begin{array}{c}\Pr(\gamma_{kn} \geq T_m, L_k(n^-) \leq \gamma_{kn^-} < U_k(n^-),\\ \ldots, L_k(n^+) \leq \gamma_{kn^+} < U_k(n^+))\end{array}}{\begin{array}{c}\Pr(L_k(n^-) \leq \gamma_{kn^-} < U_k(n^-),\\ \ldots, L_k(n^+) \leq \gamma_{kn^+} < U_k(n^+))\end{array}}. \tag{15}$$

This approach exploits the decay in correlation between the subband gains as the frequency separation between the subbands increases.

To express $\Psi_{kn}^{(m)}(\mathbf{D}_k, w)$ in a compact closed-form, let $N = n^+ - n^-$, $\tau(\nu_1, \ldots, \nu_{N-1}) = [\Gamma(d_k + \nu_1) \cdots \Gamma(d_k + \nu_{N-1})\nu_1! \cdots \nu_{N-1}!]^{-1}$, $\mathcal{G}(y, a) = \int_0^y x^{a-1} e^{-x} dx$ be the lower incomplete gamma function [30, (8.350)], and

$$\Theta_i(T) = \mathcal{G}\left(\frac{d_k(1+\rho^2)T}{\bar{\gamma}_k(1-\rho^2)}, \nu_{i-n^-} + \nu_{i-n^-+1} + d_k\right), \tag{16}$$

$$\Phi(T) = \mathcal{G}\left(\frac{d_k T}{\bar{\gamma}_k(1-\rho^2)}, \nu_1 + d_k\right), \tag{17}$$

$$\Upsilon(T) = \mathcal{G}\left(\frac{d_k T}{\bar{\gamma}_k(1-\rho^2)}, \nu_{N-1} + d_k\right). \tag{18}$$

Result 1: For subband n, the feedback-conditioned goodput $\Psi_{kn}^{(m)}(\mathbf{D}_k, w)$ for MCS m equals

$$\Psi_{kn}^{(m)}(\mathbf{D}_k, w) \approx \begin{cases} r_m \frac{C_m^{(k)}(n)}{D^{(k)}(n)}, & T_m < U_k(n), \\ 0, & \text{else,} \end{cases} \tag{19}$$

where $C_m^{(k)}(n)/D^{(k)}(n)$ is the probability of $\gamma_{kn} \geq T_m$ conditioned on the event $L_k(n^-) \leq \gamma_{kn^-} < U_k(n^-), \ldots, L_k(n^+) \leq \gamma_{kn^+} < U_k(n^+)$. Here,

$$
\begin{aligned}
D^{(k)}(n) = & \sum_{t=0}^{\infty} \rho^{2t} \sum_{\substack{\nu_1 \geq 0, \ldots, \nu_{N-1} \geq 0, \\ \nu_1 + \cdots + \nu_{N-1} = t}} \tau(\nu_1, \ldots, \nu_{N-1}) \\
& \times \frac{[\Phi(U_k(n^-)) - \Phi(L_k(n^-))]}{[\Upsilon(U_k(n^+)) - \Upsilon(L_k(n^+))]^{-1}} \\
& \times \left[\prod_{i=n^-+1}^{n^+-1} \frac{\Theta_i(U_k(i)) - \Theta_i(L_k(i))}{(1+\rho^2)^{\nu_{i-n^-}+\nu_{i-n^-+1}+d_k}} \right]. \quad (20)
\end{aligned}
$$

And, $C_m^{(k)}(n)$, for $2 \leq n \leq B-1$, is given by

$$
\begin{aligned}
C_m^{(k)}(n) = & \sum_{t=0}^{\infty} \rho^{2t} \sum_{\substack{\nu_1 \geq 0, \ldots, \nu_{N-1} \geq 0, \\ \nu_1 + \cdots + \nu_{N-1} = t}} \tau(\nu_1, \ldots, \nu_{N-1}) \\
& \times \frac{[\Theta_n(U_k(n)) - \Theta_n(\max\{T_m, L_k(n)\})]}{(1+\rho^2)^{\nu_{n-n^-}+\nu_{n-n^-+1}+d_k}} \\
& \times \frac{\Phi(U_k(n^-)) - \Phi(L_k(n^-))}{[\Upsilon(U_k(n^+)) - \Upsilon(L_k(n^+))]^{-1}} \\
& \times \left[\prod_{\substack{i=n^-+1, \\ i \neq n}}^{n^+-1} \frac{\Theta_i(U_k(i)) - \Theta_i(L_k(i))}{(1+\rho^2)^{\nu_{i-n^-}+\nu_{i-n^-+1}+d_k}} \right]. \quad (21)
\end{aligned}
$$

For the boundary cases of $n = 1$ and $n = B$, the expressions for $C_m^{(k)}(1)$ and $C_m^{(k)}(B)$ are similar to the expression for $D^{(k)}(n)$ in (20) and can be obtained by modifying it as follows. The expression for $C_m^{(k)}(1)$ is obtained by replacing $\Phi(L_k(n^-))$ in (20) by $\Phi(\max\{L_k(1), T_m\})$. The expression for $C_m^{(k)}(B)$ is obtained by replacing $\Upsilon(L_k(n^+))$ in (20) by $\Upsilon(\max\{L_k(B), T_m\})$.

Proof: The proof is given in Appendix A. ∎

2) Comments: We make the following comments:

- The notation in it is involved because it accounts for the range in which each subband's SNR lies. Furthermore, the expressions depend on the subband index n.
- The infinite series in (20) and (21) arise due to the infinite series in the joint PDF in (14). At most 70 terms of the series are sufficient for ensuring numerical accuracy for ρ as large as 0.9, with far fewer terms needed for smaller ρ.
- The complexity of evaluating the inner summation in (20) and (21) is $\mathcal{O}\left(\binom{2N_w+t-1}{t}\right)$. For example, for $B = 10$ and $t = 30$, we need to compute only 31 terms for $N_w = 1$. This is much smaller compared to $\binom{B+t-2}{t} = 4.9 \times 10^7$ terms needed for the exact computation.
- The same expressions apply to any arbitrary correlation model for $N_w = 1$. This is because the bi-variate and tri-variate PDFs of the given subband SNR and the adjacent subband SNRs that are needed in (20) and (21) are special cases of (14) for any correlation model. This also enables Rician fading to be incorporated into our model.
- The expression for $\Psi_{kn}^{(m)}(\mathbf{D}_k, w)$ in (19) is similar in form to [20, (3)]. However, there are two key differences: (i) Given b_{kn}, the quantization regions indicated by the

feedback bits are fixed in the scheme considered in [20]. However, with differential feedback, these regions are determined by W_k and change in every feedback instance. (ii) The expressions for $C_m^{(k)}(n)$ and $D^{(k)}(n)$ above use a simpler windowing-based approach, unlike [20].

B. Scenario With Path-Loss, Small-Scale Fading, Large-Scale Shadowing, and Noise

In this scenario, the expression for the post-processing SNR γ_{kn} for SIMO with MRC, MISO with MRT, and single-stream MIMO with SVD-based beamforming [31] changes to

$$
\gamma_{kn} = \frac{P_T \omega_k \phi_{kn}}{P_N}, \quad (22)
$$

where ϕ_{kn} is a gamma RV (cf. Section III-A), and ω_k models the path-loss and shadowing. As before, the term $\Omega_k' = P_T \omega_k / P_N$ is a lognormal RV with dB-mean $\mu_{\Omega_k'} = \mu_{\omega_k}(x_k) + \xi \log(P_T/P_N)$ and dB-standard deviation $\sigma_{\Omega_k'} = \sigma_{\text{shad}}$, where $\xi = 10/\log(10)$.

With shadowing, evaluating (10) is again intractable. To address this, we observe that the shadowing is the same for all subbands. We apply the intuition that given the wideband CQI $W_k = w$, limited additional information about $\tilde{S}_{kn}^*$ is conveyed by the feedback bits for subbands other than n. Consequently, (11) simplifies to

$$
\begin{aligned}
& \Psi_{kn}^{(m)}(\mathbf{D}_k, w) \\
& \approx r_m \frac{\Pr(\gamma_{kn} \geq T_m, L_k(n) \leq \gamma_{kn} < U_k(n), W_k = w)}{\Pr(L_k(n) \leq \gamma_{kn} < U_k(n), W_k = w)}. \quad (23)
\end{aligned}
$$

Note that this is different from the approach in (13), which dropped the conditioning on $W_k = w$ and retained all other terms. We shall see in Section IV-C that the above approximation is tight for all SNRs and for all ρ between 0 and 0.95. It yields the following result.

Result 2: Given the wideband and differential CQIs, $\Psi_{kn}^{(m)}(\mathbf{D}_k, w)$ is given by

$$
\Psi_{kn}^{(m)}(\mathbf{D}_k, w) \approx \begin{cases} \frac{r_m E_m(w,n)}{G(w,n)}, & T_m < U_k(n), \\ 0, & T_m \geq U_k(n), \end{cases} \quad (24)
$$

where $E_m(w,n)$ is the joint probability of the events $\gamma_{kn} \geq T_m, L_k(n) \leq \gamma_{kn} < U_k(n)$, and $W_k = w$, and $G(w,n)$ is the joint probability of the events $L_k(n) \leq \gamma_{kn} < U_k(n)$ and $W_k = w$. They are given by

$$
\begin{aligned}
E_m(w,n) = & \Pr\left(\zeta_k^{(w)} \geq T_w, \gamma_{kn} \geq \max\{T_m, L_k(n)\}\right) \\
& - \Pr\left(\zeta_k^{(w)} \geq T_w, \gamma_{kn} \geq U_k(n)\right) \\
& - \Pr\left(\zeta_k^{(w+1)} \geq T_{w+1}, \gamma_{kn} \geq \max\{T_m, L_k(n)\}\right) \\
& + \Pr\left(\zeta_k^{(w+1)} \geq T_{w+1}, \gamma_{kn} \geq U_k(n)\right), \quad (25)
\end{aligned}
$$

$$
\begin{aligned}
G_m(w,n) = & \Pr\left(\zeta_k^{(w)} \geq T_w, \gamma_{kn} \geq L_k(n)\right) \\
& - \Pr\left(\zeta_k^{(w)} \geq T_w, \gamma_{kn} \geq U_k(n)\right) \\
& - \Pr\left(\zeta_k^{(w+1)} \geq T_{w+1}, \gamma_{kn} \geq L_k(n)\right) \\
& + \Pr\left(\zeta_k^{(w+1)} \geq T_{w+1}, \gamma_{kn} \geq U_k(n)\right). \quad (26)
\end{aligned}
$$

Furthermore, for $w = M$, $\Pr\left(\zeta_k^{(w+1)} \geq T_{w+1}, \gamma_{kn} \geq g\right) = 0$, for all g.

Proof: The proof is given in Appendix B. ∎

All the probability terms in $E_m(w, n)$ and $G(w, n)$ are of the form $\Pr\left(\zeta_k^{(l)} \geq T_l, \gamma_{kn} \geq g\right)$. Notice here that the effective SINR $\zeta_k^{(l)} = -\beta_l \log\left((1/B) \sum_{n=1}^{B} \exp\left(-\gamma_{kn}/\beta_l\right)\right)$ depends on γ_{kn}. Using the steps in [11, (16)–(32)], which we summarize below, it can be written in closed-form. We do not show the detailed derivations to conserve space.

- *Step 1:* $\Pr\left(\zeta_k^{(l)} \geq T_l, \gamma_{kn} \geq g\right)$ is written as $\int_g^\infty$ $\Pr\left(\zeta_k^{(l)} \geq T_l | \gamma_{kn} = v\right) \int_0^\infty f_{\Omega'_k}(u) \frac{1}{u} f_{\phi_{kn}}(v/u) du dv$, where $f_{\Omega'_k}(\cdot)$ is the PDF of the lognormal RV Ω'_k and $f_{\phi_{kn}}(\cdot)$ is the PDF of the gamma RV ϕ_{kn}. Then, Gauss-Hermite quadrature [32, (25.4.46)] is used to simplify the inner integral.

- *Step 2:* $\Pr\left(\zeta_k^{(l)} \geq T_l | \gamma_{kn} = v\right)$ is evaluated in terms of the CDF of a Beta RV with parameters a_{li} and b_{li}, which are given below. The Beta RV arises because the term $(1/B) \sum_{n=1}^{B} \exp\left(-\gamma_{kn}/\beta_l\right)$, which is inside the exponential of the expression for the effective SNR $\zeta_k^{(l)}$ in (5), can be accurately approximated by it [28].

- *Step 3:* The Beta CDF is substituted in the outer integral in *Step 1*. Then, variable transformations, generalized Gauss-Laguerre quadrature [33], and simplifications yield the following expression for $\Pr\left(\zeta_k^{(l)} \geq T_l, \gamma_{kn} \geq g\right)$:

$$
\Pr\left(\zeta_k^{(l)} \geq T_l, \gamma_{kn} \geq g\right) \approx \frac{1}{\Gamma(d_k)\sqrt{\pi}} \sum_{i=1}^{\mathsf{GH}} z_i e^{\frac{-g}{\Lambda(\alpha_i)\varphi_k}}
$$

$$
\times \sum_{p=0}^{d_k-1} \binom{d_k-1}{p} \left(\frac{g}{\Lambda(\alpha_i)\varphi_k}\right)^{d_k-1-p} \sum_{j=1}^{\mathsf{GL}} \tilde{z}_j^{(p)}
$$

$$
\times \mathcal{B}\left(\frac{B}{B-1} e^{\frac{-T_l}{\beta_l}} - \frac{1}{B-1} e^{\frac{-\left(\varphi_k \tilde{\alpha}_j^{(p)} \Lambda(\alpha_i) + g\right)}{\beta_l}}; a_{li}, b_{li}\right),
$$

(27)

where $\Lambda(x) = \exp\left(\left(\sqrt{2}\sigma_{\Omega'_k} x + \mu_{\Omega'_k}\right)/\xi\right)$, $\mathcal{B}(x; a, b) = \frac{\int_0^x z^{a-1}(1-z)^{b-1} dz}{\int_0^1 z^{a-1}(1-z)^{b-1} dz}$ is the regularized incomplete Beta function [30, (8.392)], $\tilde{z}_j^{(p)}$ and $\tilde{\alpha}_j^{(p)}$, for $1 \leq j \leq \mathsf{GL}$, are the weights and abscissas, respectively, of generalized Gauss-Laguerre quadrature [33], and z_i and α_i, for $1 \leq i \leq \mathsf{GH}$, are the weights and abscissas, respectively, of Gauss-Hermite quadrature [32, (25.4.46)].[4] The parameters a_{li} and b_{li} in (27), which define the Beta

---

[4]Generalized Gauss-Laguerre quadrature replaces the integral $\int_0^\infty x^m e^{-x} f(x) dx$ with the finite summation $\sum_{j=1}^{\mathsf{GL}} \tilde{z}_j^{(m)} f\left(\tilde{\alpha}_j^{(m)}\right)$. Gauss-Hermite quadrature replaces the integral $\int_0^\infty e^{-x^2} f(x) dx$ with $\sum_{i=1}^{\mathsf{GH}} z_i f(\alpha_i)$. We have found $\mathsf{GL} = 8$ and $\mathsf{GH} = 10$ to be sufficient to ensure numerical accuracy for the system parameter values of interest.

PDF [28], are given by

$$
a_{li} = \frac{\mu_{li}}{V_{li}} \left[\mu_{li} - (\mu_{li})^2 - V_{li}\right],
$$

(28)

$$
b_{li} = \frac{1 - \mu_{li}}{V_{li}} \left[\mu_{li} - (\mu_{li})^2 - V_{li}\right].
$$

(29)

Here, μ_{li} and V_{li} are the mean and variance, respectively, of the Beta RV, and are given by

$$
\mu_{li} = \left(1 + \Lambda(\alpha_i)\varphi_k \beta_l^{-1}\right)^{-d_k},
$$

(30)

$$
V_{li} = \frac{1}{B-1} \left[\left(1 + 2\Lambda(\alpha_i)\varphi_k \beta_l^{-1}\right)^{-d_k} - (\mu_{li})^2\right].
$$

(31)

Extension to Multi-Stream and MU-MIMO Modes: The expression for $\Psi_{kn}^{(m)}(\mathbf{D}_k, w)$ in (24) is also applicable to the following multi-stream single user (SU)-MIMO and MU-MIMO modes:

- For the vertical Bell labs' layered space-time (V-BLAST) receiver architecture [11] with $N_r \geq N_t$, the BS transmits N_t streams of data to user k on subband n. To cancel the inter-stream interference, the received signal for stream j is multiplied with the jth row of $\mathbf{A}_{kn} \mathbf{H}_{kn}^\dagger$, where $\mathbf{A}_{kn} = \left(\mathbf{H}_{kn}^\dagger \mathbf{H}_{kn}\right)^{-1}$. The SINR $\gamma_{kn}(j)$ of user k for subband n and stream j is given by

$$
\gamma_{kn}(j) = \frac{P_T(j)\omega_k \phi_{kn}(j)}{P_N(j)} = \Omega_k(j)\phi_{kn}(j), \quad (32)
$$

where $P_T(j)$ and $P_N(j)$ are the transmit power of the BS and the AWGN power, respectively, for stream j, $\phi_{kn}(j) = 1/\mathbf{A}_{kn}(j, j)$ is a gamma RV with parameters $d_k = N_r - N_t + 1$ and $\varphi_k = 1$ [26], [34], and $\Omega_k(j) = P_T(j)\omega_k/P_N(j)$ is a lognormal RV with parameters $\mu_{\Omega_k(j)} = \mu_{\omega_k}(x_k) + \xi \log\left(P_T(j)/P_N(j)\right)$ and $\sigma_{\Omega_k(j)} = \sigma_{\text{shad}}$. The key point to note is that $\gamma_{kn}(j)$ has the same form as (22). Therefore, Result 2 and its subsequent simplifications apply.

- Similarly, for MU-MIMO with zero-forcing precoding and V-BLAST with MRC, the SINR expressions can again be written as the product of a lognormal RV and a gamma RV [11]. Hence, Result 2 and its subsequent simplifications apply.

C. Scenario With Path-Loss, Small-Scale Fading, Large-Scale Shadowing, Co-Channel Interference, and Noise

In this scenario, a user experiences path-loss, small-scale fading, large-scale shadowing, co-channel interference from neighboring cells, and noise on every subband. The derivation of $\Psi_{kn}^{(m)}(\mathbf{D}_k, w)$ is different for SIMO with MRC and for MISO with MRT because their interference statistics are different.

1) SIMO With MRC: Recall from (1) that $\gamma_{kn} = \frac{P_T \omega_k}{P_N \varepsilon_{kn}} \phi_{kn}$. Here, $\phi_{kn} = \sum_{i=1}^{N_r} |H_{kn}(i, 1)|^2$ is a gamma RV with parameters $d_k = N_r$ and $\varphi_k = 1$ [26]. And, $\varepsilon_{kn} = \frac{P_T}{P_N} \sum_{c=1}^{C} \omega_{ck} |I_{kn}(c)|^2 + 1$. For MRC, $I_{kn}(c) = \left(\sum_{j=1}^{N_r} (H_{kn}(j, 1))^* H_{kn}^{(c)}(j, 1)\right) / \sqrt{\sum_{j=1}^{N_r} |H_{kn}(j, 1)|^2}$. It can be shown to be a circularly-symmetric complex Gaussian RV with unit variance [35]. ε_{kn} is now a sum

of C lognormal RVs, which are modulated by exponential RVs, and unity, which arises due to the noise term. It is well approximated by a lognormal RV with parameters $\mu_{\varepsilon_{kn}}$ and $\sigma_{\varepsilon_{kn}}$ [11]. These parameters are obtained by the moment generating function (MGF)-matching method [17]. Since $\omega_k/\varepsilon_{kn}$ is a lognormal RV, Ω_k in (2) is a lognormal RV with parameters $\mu_{\Omega_k} = \mu_{\omega_k}(x_{0k}) - \mu_{\varepsilon_{kn}} + \xi \log(P_T/P_N)$ and $\sigma_{\Omega_k} = \sqrt{\sigma_{\omega_k}^2 + \sigma_{\varepsilon_{kn}}^2}$.

Computation of $\Psi_{kn}^{(m)}(\mathbf{D}_k, w)$: Since γ_{kn} is a product of a lognormal RV and a gamma RV, it has the same form as (22). Therefore, Result 2 and its subsequent simplifications apply.

2) MISO With MRT: In this case, $\phi_{kn} = \left(\sum_{j=1}^{N_t} |H_{kn}(1,j)|^2\right)^2$ is the square of a gamma RV with parameters $d_k = N_t$ and $\varphi_k = 1$, and $I_{kn}(c) = \sum_{j=1}^{N_t} \left(H_{sn}^{(c)}(1,j)\right)^* H_{kn}^{(c)}(1,j)$, where s is the user scheduled on subband n in cell c. This is because the beamforming weights used by BS c to serve the user s are proportional to $H_{sn}^{(c)}(1,j)$, for $1 \le j \le N_t$. Here, ε_{kn} in (3) is a sum of C lognormal RVs, which are modulated by small-scale fading related RVs, and unity. We approximate $(P_T/P_N)\omega_{ck}|I_{kn}(c)|^2$, for each c, by a lognormal RV whose parameters $\mu'_{\omega_{ck}}$ and $\sigma'_{\omega_{ck}}$ are obtained using the Fenton-Wilkinson method [22, Ch. 3].[5] As before, ε_{kn} is approximated as a lognormal RV using the MGF-matching method.

Computation of $\Psi_{kn}^{(m)}(\mathbf{D}_k, w)$: One key difference in this case compared to SIMO with MRC in Section III-C.1 is that the RV ϕ_{kn} is the square of a gamma RV. While the general expression for $\Psi_{kn}^{(m)}(\mathbf{D}_k, w)$ in (24) still applies, the probability terms $\Pr\left(\zeta_k^{(l)} \ge T_l, \gamma_{kn} \ge g\right)$ in it have to be computed differently. The final expression for it is derived in Appendix C.

Deriving tractable expressions for $\Psi_{kn}^{(m)}(\mathbf{D}_k, w)$ for single-stream MIMO with beamforming and for multi-stream MIMO modes in this scenario is an open problem.

IV. PERFORMANCE EVALUATION AND BENCHMARKING

We now present Monte Carlo simulation results for all the aforementioned scenarios. We consider a hexagonal cellular layout with $C = 6$ co-channel interfering cells around the reference cell. The cell radius is 300 m and the frequency-reuse factor is one. The simulation results are averaged over 2000 realizations of small-scale fading and large-scale shadowing (if applicable). The path-loss parameters are $\eta = 3.5$, $x_0 = 30$ m, and $\delta_{\text{dB}}(x_0) = 10$ dB. For discrete rate adaptation, we use the MCS set in [2, Table 10.1], which is common to LTE and 5G. The decoding thresholds T_m and the scaling constants β_m, for $1 \le m \le 16$, are as per [36, Table 1]. The decoding thresholds range from -9.5 dB to 19.8 dB, while the scaling constants range from 1 to 28.

---

[5]Note that the MGF-matching method is not used here because the MGF of the RV $(P_T/P_N)\omega_{ck}|I_{kn}(c)|^2$ is not known in closed-form. However, the mean and variance of the RV, which are all that the Fenton-Wilkinson method requires, can be easily derived.

A. Benchmarking Schemes

We compare with the following combinations of feedback schemes and MCS selection rules, which have been employed in several works in the literature:

- *Full Channel State Information (CSI) Feedback [4], [6]–[9]:* In it, for each subband, the user feeds back as CQI the 4-bit index of the highest-rate MCS that it can reliably decode on that subband. No differential encoding is used. Given the CQI, the BS transmits using the same MCS. It has a total feedback overhead of $4B$ bits/user. It gives an upper limit for the throughput achievable with any subband-level CQI feedback scheme.

- *HLCS Feedback [2]–[4], [11]:* In this differential feedback scheme, $b_{kn} = 2$ bits for all subbands. The differential encoding is done as per Table I. It has a total feedback overhead of $(2B + 4)$ bits/user. The BS uses C-MSR to determine the MCS for each subband.

B. Scheduling in the Multi-User Setting

Since the throughput in a multi-user setting also depends on the scheduler employed by the BS, we present results for the following two popular schedulers that trade off differently between cell throughput and user fairness. These are adapted for the TOMS rule as follows. First, we recall the following notation. The SINR of subband n of user k is γ_{kn}. The optimal MCS for this subband, as per (8), is $\tilde{S}_{kn}^*$. It has a decoding threshold $T_{\tilde{S}_{kn}^*}$, rate $r_{\tilde{S}_{kn}^*}$, and a feedback-conditioned goodput $\Psi_{kn}^{(\tilde{S}_{kn}^*)}(\mathbf{D}_k, w) = r_{\tilde{S}_{kn}^*} \Pr\left(\gamma_{kn} > T_{\tilde{S}_{kn}^*} | \mathbf{D}_k, W_k = w\right)$.

1) Round-Robin (RR) Scheduler: It allocates subbands to users in a fixed, channel-agnostic manner. For instance, in the first scheduling interval, all subbands are allocated to the first user. In the second scheduling interval, all subbands are allocated to the second user, and so on.

2) Modified Proportional Fair (MPF) Scheduler [10]: It allocates subband n to the user i_n that has the highest ratio of feedback-conditioned goodput to its mean value $\bar{\Psi}_{kn}$. Hence,

$$i_n = \arg\max_{1 \le k \le K} \left\{ \frac{\Psi_{kn}^{(\tilde{S}_{kn}^*)}(\mathbf{D}_k, w)}{\bar{\Psi}_{kn}} \right\}. \tag{33}$$

This scheduler exploits multi-user diversity and ensures fairness.

In the multi-user simulations, we also average over 200 independent user drops of K users, whose locations are distributed uniformly in the reference cell except in a circular area of radius 30 m around the BS [5]. The shadowing is generated independently for each link as per the lognormal distribution, and is different for different links. Even for a given user, the shadowing of its signal and individual interference components are different.

C. Scenarios Without Co-Channel Interference

1) Assessing the Accuracy of Results 1 and 2: Fig. 2 plots the throughput per subband that is achieved by the TOMS rule as a function of the correlation coefficient ρ between the subband small-scale fading gains for a single user for $B = 5$. The OBP used is $(1, 1, 1, 1, 1)$. This is done for
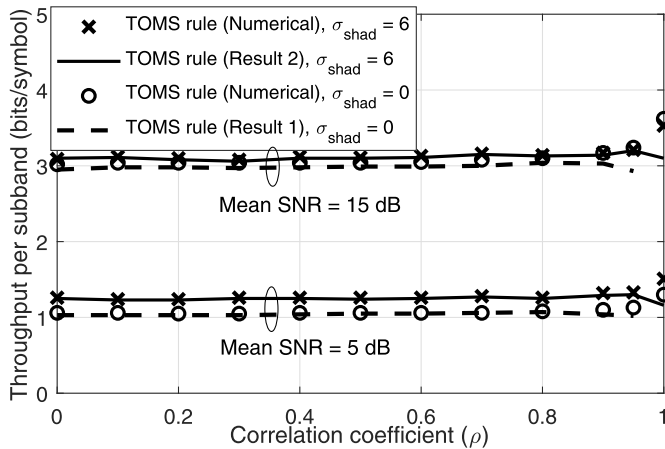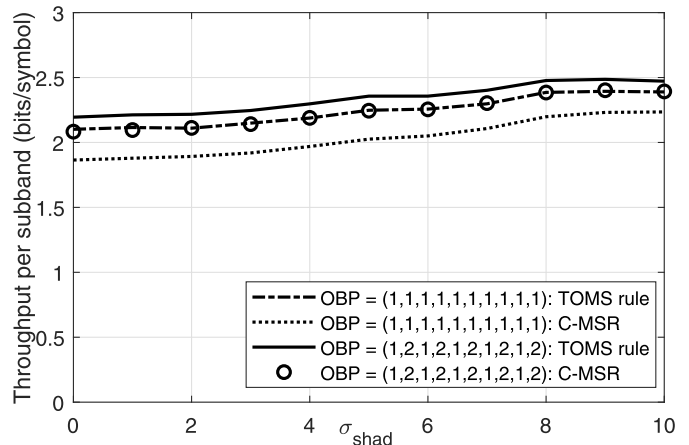
Fig. 2. Throughput per subband as a function of correlation coefficient ρ for a user that uses an OBP of $(1, 1, 1, 1, 1)$ for different mean SNRs ($B = 5$, $N_t = 1$, and $N_r = 2$).

SIMO at two mean SNRs and two σ_{shad} values. For $\sigma_{\text{shad}} = 0$, the throughput-optimal MCS is determined using Result 1, while for $\sigma_{\text{shad}} = 6$, it is determined using Result 2. For $\sigma_{\text{shad}} = 0$, results are shown only up to $\rho = 0.95$ because the presence of $1 - \rho^2$ term in (20) and (21) makes accurate numerical computation difficult as ρ approaches 1. Also shown are the results when $\Psi_{kn}^{(m)}(\mathbf{D}_k, w)$ is computed numerically from (11). For this, we generate 10^6 channel realizations for each mean SNR and σ_{shad} value. The probability term in the numerator of (11) is determined by measuring the fraction of realizations in which the corresponding event occurs. Similarly, the probability term in the denominator of (11) is also determined. We see that Result 1 is accurate over a wide range of ρ from 0 to 0.9. Similarly, Result 2 is accurate from $\rho = 0$ to $\rho = 0.95$. We also see that as $\rho \to 1$, the throughput increases. This is because as $\rho \to 1$, the MCSs on all subbands are equal with probability 1 and are equal to the wideband MCS. In this case, the throughput equals that of full CSI feedback.

2) Effect of Shadowing: Fig. 3 plots the average throughput of the TOMS rule and C-MSR as a function of σ_{shad} for a user that has a mean SNR of 10 dB at $\sigma_{\text{shad}} = 0$. Results are shown for OBPs $(1, 1, 1, 1, 1, 1, 1, 1, 1, 1)$ and $(1, 2, 1, 2, 1, 2, 1, 2, 1, 2)$ for single-stream MIMO in Fig. 3(a) and for MISO in Fig. 3(b). We set $\rho = 0.86$, which is the correlation coefficient between adjacent subband gains for the typical urban (TU) channel model [22, Ch. 1]. The TOMS rule outperforms C-MSR for all σ_{shad} for both multi-antenna modes. This is because the TOMS rule, which exploits the correlation between the wideband and subband CQIs, typically chooses a higher rate MCS compared to C-MSR. However, the TOMS rule requires more computations at the BS than C-MSR. The throughputs increase as σ_{shad} increases because the mean of the lognormal RV Ω_k' is proportional to $\exp\left(\sigma_{\Omega_k'}^2/2\right)$, which increases as σ_{shad} increases. Similar observations also hold for other OBPs and other multi-antenna modes.

3) Comparison With Imperfect CSI: Fig. 4 investigates the impact of imperfect estimates at the receiver and feedback delays. It plots the average throughput of the two rules as a function of σ_{shad} for SIMO for the following three cases:

(a) Single-stream MIMO ($N_t = 2$ and $N_r = 2$)
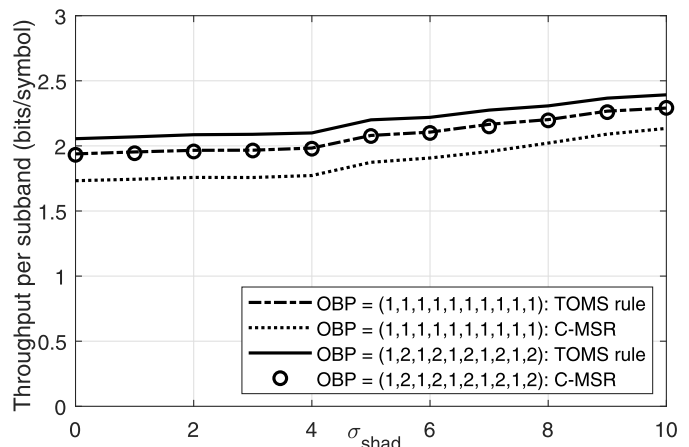
(b) MISO ($N_t = 2$ and $N_r = 1$)

Fig. 3. Throughput per subband as a function of σ_{shad} for a user that has a mean SNR of 10 dB for different OBPs and MIMO modes ($\rho = 0.86$ and $B = 10$).

(i) With perfect channel estimates at the receiver and no feedback delay; (ii) With imperfect channel estimates at the receiver, in which the wideband CQI and differential CQI are both generated based on the imperfect channel estimates and the BS determines the MCS on the basis of this imperfect CQI;[6] and (iii) With imperfect channel estimates and feedback delay, in which the BS receives the above imperfect CQI and transmits after a delay. Figs. 4(a) and 4(b) plot the results for the OBPs $(1, 1, 1, 1, 1, 1, 1, 1, 1, 1)$ and $(1, 2, 1, 2, 1, 2, 1, 2, 1, 2)$, respectively. For both OBPs, the average throughputs of both rules decrease in the presence of imperfect channel estimates and feedback delays. In all cases, the average throughput with the TOMS rule exceeds that of C-MSR.

4) Throughput-Bit Budget Region for a User: Fig. 5 presents a different perspective by plotting the normalized throughput, which is the ratio of the throughput and the throughput of full CSI feedback, as a function of the total

---

[6]The subband channel gain is estimated as follows. There are 2 resource elements per PRB containing a downlink reference signal. Each subband consists of 3 PRBs in our simulation setup. The UE employs a linear minimum mean square estimator to estimate the subband channel gain from the 6 resource elements that carry reference signals.
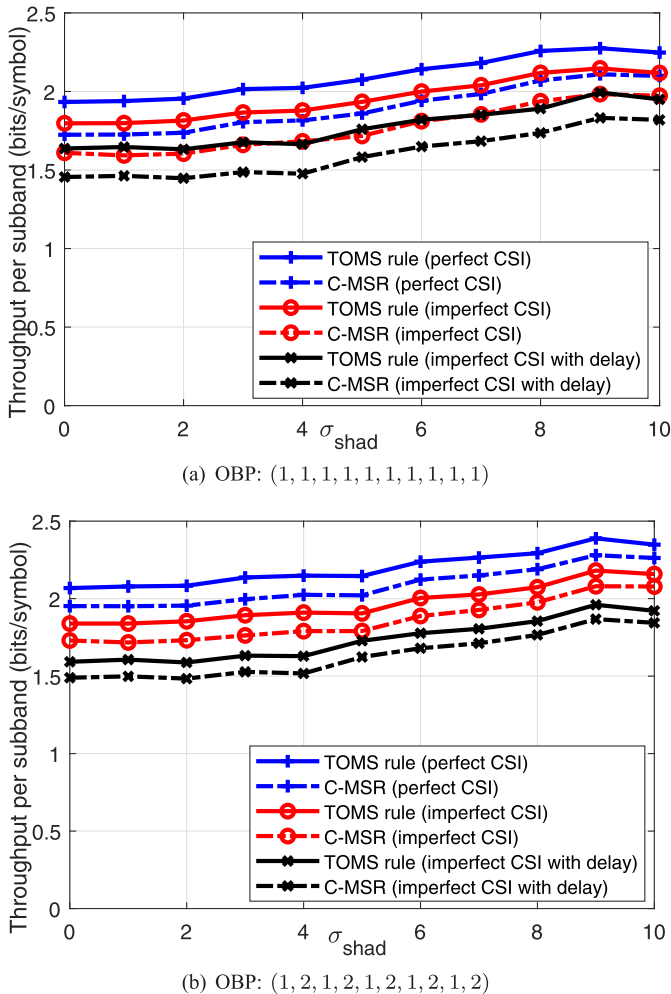
(a) OBP: $(1, 1, 1, 1, 1, 1, 1, 1, 1, 1)$

(b) OBP: $(1, 2, 1, 2, 1, 2, 1, 2, 1, 2)$

Fig. 4. Effect of imperfect channel estimates at the receiver and feedback delays: Throughput per subband as a function of σ_{shad} for a user that has a mean SNR of 10 dB (SIMO, $N_r = 2$, $\rho = 0.86$, $B = 10$, speed of 3 kmph, and delay of 8 ms).

TABLE II
BEST OBP AS A FUNCTION OF THE
TOTAL DIFFERENTIAL FEEDBACK
OVERHEAD O_k ($B = 10$)

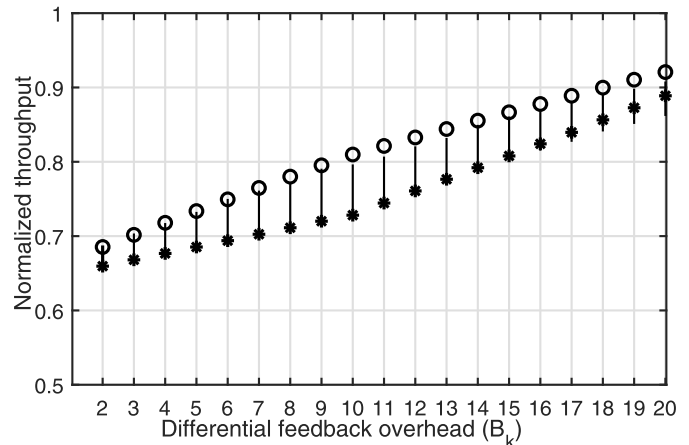| O_k (bits)	Best OBP
5	(0,1,0,1,0,1,0,1,0,1)
10	(1,1,1,1,1,1,1,1,1,1)
12	(1,2,1,1,1,1,1,1,2,1)
15	(1,2,1,2,1,2,1,2,1,2)
20	(2,2,2,2,2,2,2,2,2,2)

Fig. 5. Normalized throughput as a function of O_k (bits) for different OBPs ($\sigma_{\text{shad}} = 6$, mean SNR of 15.3 dB, $\rho = 0$, $B = 10$, and SIMO with $N_r = 2$). The normalized throughput of the best OBP that maximizes the throughput is shown using the marker '○'. For the best OBP, the normalized throughput with C-MSR is shown using the marker '∗'. For each value of O_k, the vertical line shows the spread in the throughputs achieved by 20 randomly chosen OBPs.

differential feedback overhead O_k. It enables us to visually assess the efficacy of many OBPs and the gains from using the TOMS rule. The many values that O_k can take show the new flexibility available to the BS to control the uplink feedback overhead. This is done for the scenario with path-loss, small-scale fading, large-scale shadowing, and noise. For each O_k, the normalized throughput of the OBP that maximizes the throughput is shown using the marker '○'.[7] For this best OBP, the normalized throughput with C-MSR is shown using the marker '∗'. Also shown are the range of values of the normalized throughputs that are achieved by 20 randomly chosen OBPs with the TOMS rule and C-MSR. Since they are sub-optimal, their normalized throughputs lie in a black vertical line below that of the optimal OBP. For $O_k = 20$ bits and $B = 10$, the best OBP turns out to be the same as that of the HLCS feedback scheme. However, for other values of O_k, it is different. For example, it is $(1, 1, 1, 1, 1, 1, 1, 1, 1, 1)$ for

[7]The OBP is found using a greedy search algorithm. It starts from an all-zero OBP that has $O_k = 0$ bits. In each iteration, it increments O_k by 1, computes the throughput via Monte Carlo simulations for each of the B OBPs that arise for the B locations of this bit, and selects the OBP that maximizes the average sum throughput.

$O_k = 10$ bits and $(1, 2, 1, 2, 1, 2, 1, 2, 1, 2)$ for $O_k = 15$ bits. The best OBPs for different O_k are tabulated in Table II.

As O_k increases, the normalized throughputs of both MCS selection rules increase and tend towards 1 since more CSI is fed back. The TOMS rule outperforms C-MSR for all O_k. The difference between the two is the most when O_k is between 5 and 15 bits. The proposed approach yields 80% of full CSI feedback's throughput at a total feedback overhead of 13 bits. This is only 32.5% of the 40-bit overhead of full CSI feedback. Furthermore, it yields 90% of full CSI feedback's throughput with a total feedback overhead of only 22 bits.

5) Multi-User Case: Fig. 6 plots the cell throughput of the different feedback schemes and MCS selection rules as a function of σ_{shad} for the MPF and RR schedulers for SIMO with $K = 5$ users. This is done for the scenario with path-loss, small-scale fading, large-scale shadowing, and noise. Results are shown for $O_k = 12$ bits, for which the best OBP is $(1, 2, 1, 1, 1, 1, 1, 1, 2, 1)$. All users use the same OBP. The ratio P_T/P_N in (1) is set such that the mean cell-edge SNR is 3 dB. For $\sigma_{\text{shad}} = 0$, which corresponds to the scenario with path-loss, small-scale fading, and noise (Section III-A), the throughput is computed using Result 1 and plotted using the marker '×'.

For all values of σ_{shad} and for both schedulers, the TOMS rule outperforms C-MSR. For the MPF scheduler, the through-put increases as σ_{shad} increases. Intuitively, this occurs because the MPF scheduler exploits multi-user diversity and chooses users with higher mean SNRs in each user-drop. On the other
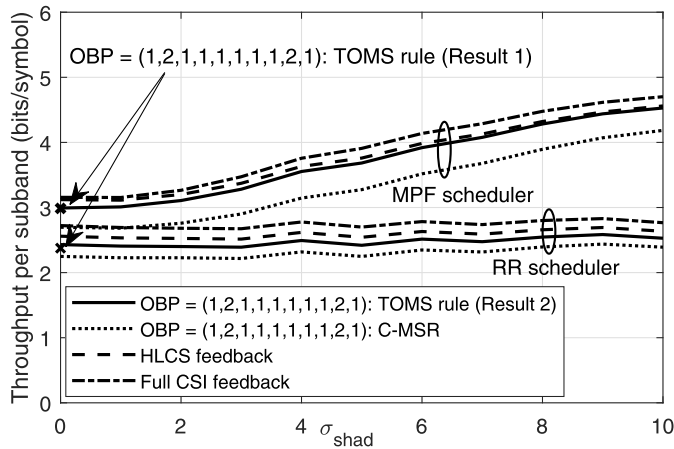
Fig. 6. Cell throughput per subband achieved by different feedback schemes and MCS selection rules as a function of the lognormal shadowing standard deviation σ_{shad} for different schedulers with $O_k = 12$ bits (cell-edge SNR of 3 dB, $\rho = 0.86$, $N_t = 1$, $N_r = 2$, $B = 10$, and $K = 5$).
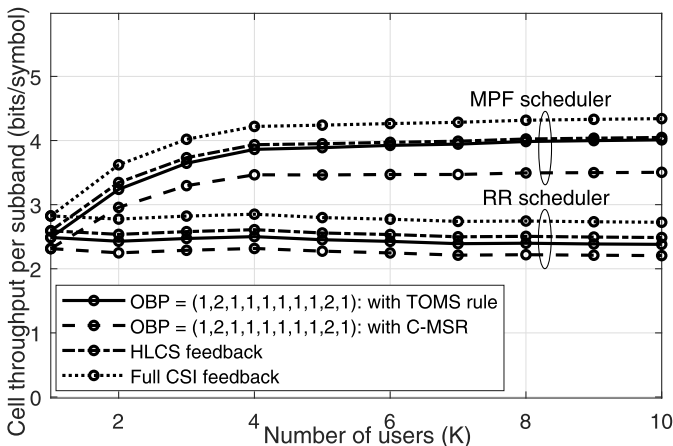

Fig. 7. Cell throughput per subband as a function of K for RR and MPF schedulers ($\sigma_{\text{shad}} = 6$, $B = 10$, $O_k = 12$ bits, and SIMO with $N_t = 1$ and $N_r = 4$).

hand, the throughput of the RR scheduler is insensitive to σ_{shad}. This is because it does not exploit multi-user diversity and does not benefit from the variation in the SNRs due to shadowing. One unexpected outcome is that Result 2 yields the same throughput for the TOMS rule as Result 1 even for $\sigma_{\text{shad}} = 0$. Thus, neglecting the frequency-domain correlation between the subband gains due to small-scale fading has a negligible impact once the correlation between the wideband and differential CQIs is accounted for.

D. Scenario With Path-Loss, Small-Scale Fading, Large-Scale Shadowing, Co-Channel Interference, and Noise

Fig. 7 plots the cell throughput per subband of the TOMS rule and C-MSR as a function of K for the OBP $(1, 2, 1, 1, 1, 1, 1, 1, 2, 1)$, for which $O_k = 12$ bits. Results are shown for the RR and MPF schedulers for SIMO. For reference, the cell throughputs of full CSI feedback and HLCS feedback are also shown. The cell throughputs of all schemes increase as K increases for the MPF scheduler, due to its ability to exploit multi-user diversity. On the other hand, the cell throughputs are insensitive to K for the RR scheduler.

As before, the TOMS rule outperforms C-MSR for both schedulers. The throughput gain is larger for the MPF scheduler than the RR scheduler, especially for larger K. The cell throughput of the TOMS rule is close to that of HLCS feedback for all K. The TOMS rule achieves this despite requiring only 66.7% of the overhead of HLCS feedback. With $K = 10$, the MPF scheduler in conjunction with the TOMS rule achieves 92.3% of the cell throughput of full CSI feedback with just 40.0% of its total feedback overhead. The corresponding value for the RR scheduler is 91.1%.

V. CONCLUSION

We proposed a novel flexible-overhead feedback scheme that used a combination of wideband CQI and differential CQI. In it the number of overhead bits for differential feedback could be different for different subbands. We also derived closed-form expressions for the feedback-conditioned goodput of an MCS as a function of the OBP, and saw that the TOMS rule selected the MCS with the largest feedback-conditioned goodput. We did so for several deployment scenarios that incorporated different combinations of small-scale fading, large-scale shadowing that was heterogeneous across links and users, co-channel interference, and multiple antenna modes. The derivations exploited the correlation between the differential and wideband CQIs to arrive at expressions with much lower computational complexity. They used novel, accurate approximations to handle the involved form of EESM and the joint PDF of the correlated subband channel gains.

We observed that the TOMS rule outperformed C-MSR. The proposed OBPs yielded significant throughput gains especially for medium feedback bit budgets. With multiple users, the proposed approach achieved nearly the same throughput as the conventional HLCS feedback scheme with much less overhead for both MPF and RR schedulers. Interesting avenues for future work include modeling frequency-selective fading within a subband and developing new learning algorithms that efficiently implement the TOMS rule for arbitrary signal and interference statistics.

APPENDIX A
BRIEF DERIVATION OF RESULT 1

The events $L_k(n) \leq \gamma_{kn} < U_k(n)$ and $\gamma_{kn} \geq T_m$ are mutually exclusive for $T_m > U_k(n)$. Hence, for $T_m \geq U_k(n)$, it follows that

$$\Pr\left(\gamma_{kn} \geq T_m, L_k(1) \leq \gamma_1 < U_k(1), \right.$$
$$\left. \ldots, L_k(B) \leq \gamma_B < U_k(B)\right) = 0, \quad (34)$$

which also implies that $\Psi_{kn}^{(m)}(\mathbf{D}_k, w) = 0$. For $T_m < U_k(n)$, $\Psi_{kn}^{(m)}(\mathbf{D}_k, w)$ can be written in terms of the joint PDF $f_{\gamma}(\cdot)$ of the vector $\gamma = (\gamma_{n^-}, \ldots, \gamma_{n^+})$ of subband SINRs as

$$\Psi_{kn}^{(m)}(\mathbf{D}_k, w)$$
$$\approx r_m \frac{\int_{L_k(n^-)}^{U_k(n^-)} \cdots \int_{\max\{T_m, L_k(n)\}}^{U_k(n)} \cdots \int_{L_k(n^+)}^{U_k(n^+)} f_{\gamma}(\mathbf{u}) \, d\mathbf{u}}{\int_{L_k(n^-)}^{U_k(n^-)} \cdots \int_{L_k(n)}^{U_k(n)} \cdots \int_{L_k(n^+)}^{U_k(n^+)} f_{\gamma}(\mathbf{u}) \, d\mathbf{u}}.$$
$$(35)$$

To compute the denominator $D^{(k)}(n)$ in (35), we substitute the PDF $f_{\boldsymbol{\gamma}}(\cdot)$ of $\gamma_{n^-}, \ldots, \gamma_{n^+}$ from (14) in (35). This yields

$$
\begin{aligned}
D^{(k)}(n) = &\int_{L_k(n^-)}^{U_k(n^-)} \cdots \int_{L_k(n)}^{U_k(n)} \cdots \int_{L_k(n^+)}^{U_k(n^+)} \frac{1}{\left(\frac{\bar{\gamma}_k}{d_k}\right)^{d_k N}} \\
&\times \frac{e^{\frac{-d_k}{\bar{\gamma}_k(1-\rho^2)}\left(u_{n^-}+u_{n^+}+(1+\rho^2)\sum_{i=n^-}^{n^+} u_i\right)}}{\Gamma(d_k)(1-\rho^2)^{d_k(N-1)}} \sum_{t=0}^{\infty} Z_k^{2t} \\
&\times \sum_{\substack{\nu_1 \geq 0,\ldots,\nu_{N-1}\geq 0 \\ \nu_1+\cdots+\nu_{N-1}=t}} \left[\prod_{j=n^-+1}^{n^+-1} \frac{(u_j)^{\nu_i+\nu_{i-1}+d_k-1}}{\nu_j \Gamma(\nu_j+d_k)} \right] \\
&\times \frac{(u_{n^+})^{\nu_{N-1}+d_k-1}}{\Gamma(\nu_1+d_k)\nu_1(u_{n^-})^{1-\nu_1-d_k}} du_{n^-} \ldots du_{n^+},
\end{aligned}
\tag{36}
$$

where $Z_k = d_k \rho/(\bar{\gamma}_k[1-\rho^2])$. Taking the integrals inside the summation, separating them out in terms of $u_{n^-}, \ldots, u_{n^+}$, and writing the resulting expression in terms of lower incomplete gamma functions yields the expression for $D^{(k)}(n)$ in (20). The integration in the numerator in (35) is also computed in a similar manner.

The expressions for the numerator for subbands $n = 1$ and $n = B$ are computed in a similar manner. They turn out to be slightly different due to two reasons. First, the limits of integration for these two boundary subbands are different from those for the other subbands. Second, in (14), the exponents of u_1 and u_B are different from those of $u_2, \ldots, u_{B-1}$.

APPENDIX B
DERIVATION OF RESULT 2

As in Appendix A, $\Psi_{kn}^{(m)}(\mathbf{D}_k, w) = 0$ for $T_m \geq U_k(n)$. For $T_m < U_k(n)$, it follows from (23) that

$$
\Psi_{kn}^{(m)}(\mathbf{D}_k, w) \approx r_m \frac{\begin{aligned}&\Pr(W_k = w, \gamma_{kn} \geq \max\{T_m, L_k(n)\}) \\ &- \Pr(W_k = w, \gamma_{kn} \geq U_k(n))\end{aligned}}{\begin{aligned}&\Pr(W_k = w, \gamma_{kn} \geq L_k(n)) \\ &- \Pr(W_k = w, \gamma_{kn} \geq U_k(n))\end{aligned}}.
\tag{37}
$$

In (37), each term in the numerator and the denominator is of the form $\Pr(W_k = w, \gamma_{kn} \geq g)$. From (6), this common form can be written as

$$
\Pr(W_k = w, \gamma_{kn} \geq g) = \Pr\left(\zeta_k^{(w)} \geq T_w, \zeta_k^{(w+1)} < T_{w+1},\right.
$$
$$
\left. \ldots, \zeta_k^{(M)} < T_M, \gamma_{kn} \geq g\right).
\tag{38}
$$

Computing it is intractable as it requires an $(M - w + 2)$-dimensional joint PDF of the RVs $\zeta_k^{(w)}, \zeta_k^{(w+1)}, \ldots, \zeta_k^{(M)}$, and γ_{kn}. It can be simplified by observing that if a user cannot decode MCS $w + 1$, then it it is highly unlikely that it can decode a higher-rate MCS. Therefore,

$$
\begin{aligned}
&\Pr(W_k = w, \gamma_{kn} \geq g) \\
&\approx \Pr\left(\zeta_k^{(w)} \geq T_w, \zeta_k^{(w+1)} < T_{w+1}, \gamma_{kn} \geq g\right),
\end{aligned}
\tag{39}
$$
$$
\begin{aligned}
&= \Pr\left(\zeta_k^{(w)} \geq T_w, \gamma_{kn} \geq g\right) \\
&- \Pr\left(\zeta_k^{(w)} \geq T_w, \zeta_k^{(w+1)} \geq T_{w+1}, \gamma_{kn} \geq g\right).
\end{aligned}
\tag{40}
$$

Similarly, if the user can decode MCS $w+1$, it is highly likely that it can also decode w. Applying this reasoning to simplify the second probability term in (40) yields

$$
\begin{aligned}
&\Pr\left(\zeta_k^{(w)} \geq T_w, \zeta_k^{(w+1)} \geq T_{w+1}, \gamma_{kn} \geq g\right) \\
&\qquad\qquad \approx \Pr\left(\zeta_k^{(w+1)} \geq T_{w+1}, \gamma_{kn} \geq g\right).
\end{aligned}
\tag{41}
$$

Combining (40) and (41), we get

$$
\begin{aligned}
\Pr(W_k = w, \gamma_{kn} \geq g) &\approx \Pr\left(\zeta_k^{(w)} \geq T_w, \gamma_{kn} \geq g\right) \\
&- \Pr\left(\zeta_k^{(w+1)} \geq T_{w+1}, \gamma_{kn} \geq g\right).
\end{aligned}
\tag{42}
$$

Applying the simplifications in (38)–(42) to each term in (37) yields (24).

APPENDIX C
$\Pr(W_k = w, \gamma_{kn} \geq g)$ FOR MISO WITH MRT

Using the approach in [11, (51)], we get

$$
\begin{aligned}
\Pr\left(\zeta_k^{(l)} \geq T_l, \gamma_{kn} \geq g\right) &\approx \frac{1}{\Gamma(d_k)\sqrt{\pi}} \sum_{i=1}^{GH} z_i e^{-g'} \\
&\times \sum_{p=0}^{d_k-1} \binom{d_k-1}{p} (g')^{d_k-1-p} \sum_{j=1}^{GL} \tilde{z}_j^{(p)} \\
&\times \mathcal{B}\left(\frac{B}{B-1} e^{\frac{-T_l}{\beta_l}} - \frac{1}{B-1} e^{\frac{-\left(\tilde{\alpha}_j^{(p)}+g'\right)^2 \varphi_k^2 \Delta(\alpha_i)^{(k)}}{\beta_l}}; a_{li}, b_{li} \right),
\end{aligned}
\tag{43}
$$

where $g' = (1/\varphi_k)\sqrt{g/\kappa(\alpha_i)}$ and $\kappa(x) = e^{\left(\sqrt{2}\sigma_{\Omega_k}x+\mu_{\Omega_k}\right)/\xi}$. The constants $\tilde{z}_j^{(p)}$, $\tilde{\alpha}_j^{(p)}$, GL, z_i, α_i, and GH have been defined in Section III-B. The parameters a_{li} and b_{li} of the Beta RVs are calculated using (28) and (29), respectively. The mean μ_{li} and variance V_{li} are

$$
\mu_{li} \approx \frac{1}{\Gamma(d_k)} \sum_{j=1}^{GL} \tilde{z}_j^{(d_k)} e^{-\frac{\varphi_k^2\left(\tilde{\alpha}_j^{(d_k)}\right)^2 \kappa(\alpha_i)}{\beta_l}},
$$

$$
V_{li} \approx \frac{1}{B-1} \left[\frac{1}{\Gamma(d_k)} \sum_{j=1}^{GL} \tilde{z}_j^{(d_k)} e^{-\frac{2\varphi_k^2\left(\tilde{\alpha}_j^{(d_k)}\right)^2 \kappa(\alpha_i)}{\beta_l}} - (\mu_{li})^2 \right].
$$

The detailed derivation is not shown here to conserve space.

REFERENCES

[1] V. Kumar and N. B. Mehta, "Exploiting correlation between wideband and differential CQIs to improve rate adaptation and reduce feedback overhead in 4G/5G systems," in *Proc. IEEE Globecom.*, Dec. 2020, pp. 1–6.

[2] S. Sesia, I. Toufik, and M. Baker, *LTE—The UMTS Long Term Evolution: From Theory to Practice*, 2nd ed. Hoboken, NJ, USA: Wiley, 2009.

[3] *NR-Physical Layer Procedures for Data*, 3rd Generation Partnership Project (3GPP), document TS 38.214, v15.2.0, 2018.

[4] A. Chiumento, M. Bennis, C. Desset, L. V. der Perre, and S. Pollin, "Adaptive CSI and feedback estimation in LTE and beyond: A Gaussian process regression approach," *EURASIP J. Wireless Commun. Netw.*, vol. 2015, no. 1, p. 168, Jun. 2015, doi: 10.1186/s13638-015-0388-0.

[5] M. Cordina and C. J. Debono, "Robust predictive filtering schemes for sub-band CQI feedback compression in 3GPP LTE systems," *IET Commun.*, vol. 11, no. 11, pp. 1797–1807, Aug. 2017.

[6] J. Duplicy *et al.*, "MU-MIMO in LTE systems," *EURASIP J. Wireless Commun. Netw.*, vol. 2011, no. 1, Mar. 2011, Art. no. 496763, doi: 10.1155/2011/496763.

[7] H. T. Nguyen, I. Z. Kovacs, Y. Wang, and K. I. Pedersen, "Feedback compression schemes for downlink carrier aggregation in LTE-advanced," in *Proc. IEEE Veh. Technol. Conf. (VTC Fall)*, Sep. 2011, pp. 1–5.

[8] Q.-T. Thieu, C. Wang, C.-H. Wang, and H.-Y. Hsieh, "Design and implementation of NOMA subband scheduling towards larger bandwidth beyond LTE–A," in *Proc. IEEE 28th Annu. Int. Symp. Pers., Indoor, Mobile Radio Commun. (PIMRC)*, Oct. 2017, pp. 1–7.

[9] A. De La Fuente, G. Femenias, F. Riera-Palou, and A. García Armada, "Subband CQI feedback-based multicast resource allocation in MIMO-OFDMA networks," *IEEE Trans. Broadcast.*, vol. 64, no. 4, pp. 846–864, Dec. 2018.

[10] S. N. Donthi and N. B. Mehta, "An accurate model for EESM and its application to analysis of CQI feedback schemes and scheduling in LTE," *IEEE Trans. Wireless Commun.*, vol. 10, no. 10, pp. 3436–3448, Oct. 2011.

[11] V. Kumar and N. B. Mehta, "Modeling and analysis of differential CQI feedback in 4G/5G OFDM cellular systems," *IEEE Trans. Wireless Commun.*, vol. 18, no. 4, pp. 2361–2373, Apr. 2019.

[12] S. Homayouni, S. Schwarz, M. K. Mueller, and M. Rupp, "Reducing CQI feedback overhead by exploiting spatial correlation," in *Proc. IEEE 87th Veh. Technol. Conf. (VTC Spring)*, Jun. 2018, pp. 1–5.

[13] Y.-S. Jeon, H.-M. Kim, Y.-S. Cho, and G.-H. Im, "Time-domain differential feedback for massive MISO-OFDM systems in correlated channels," *IEEE Trans. Commun.*, vol. 64, no. 2, pp. 630–642, Feb. 2016.

[14] W.-S. Liao, M. G. Kibria, G. P. Villardi, O. Zhao, K. Ishizu, and F. Kojima, "Coordinated multi-point downlink transmission for dense small cell networks," *IEEE Trans. Veh. Technol.*, vol. 68, no. 1, pp. 431–441, Jan. 2019.

[15] B. Yang, G. Mao, M. Ding, X. Ge, and X. Tao, "Dense small cell networks: From noise-limited to dense interference-limited," *IEEE Trans. Veh. Technol.*, vol. 67, no. 5, pp. 4262–4277, May 2018.

[16] Y. Wang and H. Cao, "Capacity bounds for Rayleigh/lognormal MIMO channels with double-sided correlation," *IEEE Commun. Lett.*, vol. 19, no. 8, pp. 1362–1365, Aug. 2015.

[17] N. Mehta, J. Wu, A. Molisch, and J. Zhang, "Approximating a sum of random variables with a lognormal," *IEEE Trans. Wireless Commun.*, vol. 6, no. 7, pp. 2690–2699, Jul. 2007.

[18] D. Ben Cheikh, J.-M. Kelif, M. Coupechoux, and P. Godlewski, "Multicellular zero forcing precoding performance in Rayleigh and shadow fading," in *Proc. IEEE 73rd Veh. Technol. Conf. (VTC Spring)*, May 2011, pp. 1–5.

[19] J. G. Proakis, *Digital Communications*, 5th ed. New York, NY, USA: McGraw-Hill, 2014.

[20] V. Kumar and N. B. Mehta, "Base station-side rate estimation for threshold-based feedback, and design implications in multi-user OFDM systems," *IEEE Trans. Wireless Commun.*, vol. 16, no. 11, pp. 7634–7645, Nov. 2017.

[21] *NR-Physical Channels and Modulation*, 3rd Generation Partnership Project (3GPP), document TS 38.211, v15.2.0, 2018.

[22] G. L. Stüber, *Principles of Mobile Communication*, 2nd ed. New York, NY, USA: Springer, 2011.

[23] A. J. Goldsmith, *Wireless Communication*, 2nd ed. Cambridge, U.K.: Cambridge Univ. Press, 2005.

[24] V. A. Aalo and T. Piboongungon, "On the multivariate generalized gamma distribution with exponential correlation," in *Proc. IEEE Global Telecommun. Conf. (GLOBECOM)*, Nov. 2005, pp. 1229–1233.

[25] J. Zhang, M. Matthaiou, G. K. Karagiannidis, and L. Dai, "On the multivariate gamma–gamma distribution with arbitrary correlation and applications in wireless communications," *IEEE Trans. Veh. Technol.*, vol. 65, no. 5, pp. 3834–3840, May 2016.

[26] X. Yu, C. Li, J. Zhang, M. Haenggi, and K. B. Letaief, "A unified framework for the tractable analysis of multi-antenna wireless networks," *IEEE Trans. Wireless Commun.*, vol. 17, no. 12, pp. 7965–7980, Dec. 2018.

[27] B. Makki and T. Eriksson, "Feedback subsampling in temporally-correlated slowly-fading channels using quantized CSI," *IEEE Trans. Commun.*, vol. 61, no. 6, pp. 2282–2294, Jun. 2013.

[28] J. Francis and N. B. Mehta, "EESM-based link adaptation in point-to-point and multi-cell OFDM systems: Modeling and analysis," *IEEE Trans. Wireless Commun.*, vol. 13, no. 1, pp. 407–417, Jan. 2014.

[29] J. C. Ikuno, M. Wrulich, and M. Rupp, "System level simulation of LTE networks," in *Proc. IEEE 71st Veh. Technol. Conf.*, May 2010, pp. 1–5.

[30] L. S. Gradshteyn and L. M. Ryzhik, *Tables of Integrals, Series and Products*, 7th ed. New York, NY, USA: Academic, 2007.

[31] Y. Li, L. Zhang, L. J. Cimini, and H. Zhang, "Statistical analysis of MIMO beamforming with co-channel unequal-power MIMO interferers under path-loss and Rayleigh fading," *IEEE Trans. Signal Process.*, vol. 59, no. 8, pp. 3738–3748, Aug. 2011.

[32] M. Abramowitz and I. Stegun, *Handbook of Mathematical Functions: With Formulas, Graphs, and Mathematical Tables*, 9th ed. New York, NY, USA: Dover, 1972.

[33] P. Rabinowitz and G. Weiss, "Tables of abscissas and weights for numerical evaluation of integrals of the form $\int_0^\infty e^{-x} X^n f(X) dx$," *Math. Tables Aids Comput.*, vol. 13, no. 68, pp. 285–294, Oct. 1959.

[34] R. H. Y. Louie, M. R. McKay, and I. B. Collings, "Open-loop spatial multiplexing and diversity communications in ad hoc networks," *IEEE Trans. Inf. Theory*, vol. 57, no. 1, pp. 317–344, Jan. 2011.

[35] A. Shah and A. M. Haimovich, "Performance analysis of maximal ratio combining and comparison with optimum combining for mobile radio communications with cochannel interference," *IEEE Trans. Veh. Technol.*, vol. 49, no. 4, pp. 1454–1463, Jul. 2000.

[36] J. Fan, Q. Yin, G. Y. Li, B. Peng, and X. Zhu, "MCS selection for throughput improvement in downlink LTE systems," in *Proc. 20th Int. Conf. Comput. Commun. Netw. (ICCCN)*, Jul. 2011, pp. 1–5.

Vineeth Kumar received the B.Tech. degree in electronics and communications engineering from Amrita University, Amritapuri, Kerala, India, in 2011, the M.Tech. degree in signal processing from the National Institute of Technology, Calicut, in 2014, and the Ph.D. degree in electrical communication engineering from the Indian Institute of Science, Bengaluru, in 2020. His research interests include the design and performance analysis of limited feedback schemes for rate adaptation and resource allocation in OFDM systems.

Neelesh B. Mehta (Fellow, IEEE) received the B.Tech. degree in electronics and communications engineering from the Indian Institute of Technology (IIT) Madras, in 1996, and the M.S. and Ph.D. degrees in electrical engineering from the California Institute of Technology, Pasadena, CA, USA, in 1997 and 2001, respectively. He is currently a Professor with the Department of Electrical Communication Engineering, Indian Institute of Science, Bangalore. He is a fellow of the Indian National Academy of Engineering (INAE), Indian National Science Academy (INSA), and the National Academy of Sciences India (NASI). He was a recipient of the Shanti Swarup Bhatnagar Award 2017 and the Swarnjayanti Fellowship. He has served on the Board of Governors of IEEE ComSoc from 2012 to 2015. He has served on the Executive Editorial Committee of the IEEE TRANSACTIONS ON WIRELESS COMMUNICATIONS from 2014 to 2017, and served as its Chair from 2017 to 2018. He also serves on the Steering Committee of the journal.